Bimetallic Pt-Pd co-catalyst Nb-doped TiO_2 materials for H_2 photo-production under UV and Visible light illumination

Uriel Caudillo-Flores,[1] Mario J. Muñoz-Batista,[1] Marcos Fernández-García[1,] Anna Kubacka[1,*]*

[1] Instituto de Catálisis y Petroleoquímica. CSIC. C/ Marie Curie, 2. 28049 Madrid, Spain.

Abstract

In this work we synthesized a series of binary PtPd co-catalysts supported on a Nb-doped TiO_2 support. The catalytic solids and corresponding monometallic reference systems are characterized using X-ray diffraction, X-ray photoelectron, and UV-visible spectroscopies, together with microscopy and porosimetry tools. Such characterization was able to show the formation of PtPd alloy particles in the bimetallic catalysts. The mono and bimetallic TiO_2-based powders were tested in the photo-production of hydrogen from methanol:water mixtures under UV and visible illumination conditions. Analysis of catalytic properties was carried out through the measurement of the optical properties of the materials and the calculation of the true quantum efficiency parameter. Results indicate that the PtPd co-catalysts have superior performance that the Pt and Pd monometallic counterparts both under UV and visible illumination conditions. Optimum performance was achieved with a material having a Pt:Pd 1:1 atomic ratio. A remarkable increase in the use of the visible range and thus in sunlight utilization is achieved with the 1:1 Pt:Pd bimetallic system with respect to the monometallic counterparts. The evolution of the bimetallic co-catalysts under reaction conditions as well as their key properties to interpret photo-activity were analyzed with the help of the above mentioned techniques as well as photoluminescence spectroscopy and an in-situ infrared analysis of the materials under reaction conditions. Results point out the critical role that both PtPd alloying and the metal-support interface play in the reaction.

KEYWORDS: Bimetallic co-catalyst, Quantum Efficiency and Yield; In-situ FTIR; UV; Visible; Sunlight

Corresponding author address: M.F.-G. (mfg@icp.csic.es), A.K. (ak@icp.csic.es)

1. Introduction

Hydrogen production from renewable sources will be an enabling technology for a better and greener future. Maturing such technology is therefore required in the quest of building up a sustainable society for the XXI century. Photocatalysis can provide an attractive alternative for the renewable production of hydrogen using exclusively light and bio-molecules as, respectively, input energy and reactants (1,2,3,4,5). Several bio-alcohols have been tested in the above mentioned process, being those having at least one hydrogen atom bonded to the (carbon) alpha position the ones rendering higher reaction rates (6,7,8,9,10,11,12,13,14,15,16,17,18). Among bio-derived alcohols, methanol is the simple one from a chemical point of view and probably the molecule receiving most attention due to the relatively high hydrogen production rates commonly observed (19,20,21,22,23,24).

Titania-based materials have been customarily used in photocatalysis due to a number of properties including their relatively low cost, relatively low toxicity and high biocompatibility, high availability, and significant activity in all reactions tested and, particularly for our purposes, in hydrogen production using bio-alcohols as sacrificial agents (1-5, 25). In photochemical and more frequently in photoelectrochemical processes, doping of titania with Nb has been used to enhance charge transport and mobility, particularly concerning electron-related species (26, 27). This aspect is potentially important in the hydrogen production process as it requires the reduction of protons by electron species to render the desired product, the hydrogen molecule.

In hydrogen photocatalytic production concerning titania based materials the use of a noble metal metallic co-catalyst has been shown to enhance significantly activity with respect to the reference semiconductor (alone) systems (1,4,28,29). Platinum is the most studied noble metal co-catalysts due to its high effectiveness. Pt and in general noble metal promotion of hydrogen photoproduction has been interpreted in the literature considering a significant number of physico-chemical phenomena including those related to morphology and associated to primary particle size, and shape of the noble metal, electron-acceptor or handling properties of the metal phase itself as well as of the metal-oxide interface. All these physico-chemical properties can have direct and beneficial effects in charge handling and, in turn, can impact the charge recombination process in a photocatalytic solid (13,15,20-22,30,31,32,33,34,35,36,37,38,39,40,41,42,43). Pt has the higher work function among noble metals, and would thus drive to a stronger electron transfer with titania. It also

displays the lowest energy for proton reduction. The two facts would make Pt a reasonable choice for the photo-generation of hydrogen (44). Nevertheless, in parallel studies the usefulness of other noble metal co-catalysts and particularly Pd has been demonstrated in several previous reports (11,40,45,46,47,48,49,50,51).

As occurs in many catalytic processes, bimetallic systems can provide the basis for increasing the activity of numerous catalytic materials. The outstanding catalytic properties of Pt have been shown to be improved through the use of PtPd bimetallic formulations in a number of photocatalytic reactions concerning the degradation of organic molecules such as phenol, CO oxidation, dehalogenation of organic halides or hydrogen production. The most active PtPd binary systems are usually Pt rich alloys, being a Pt:Pd atomic ratio of 1:1 the inferior limit for Pt content (52,53,54,55). This could be based in the significant modification of the valence d-band of alloying materials with respect to the monometallic materials, which has strong influence in the interaction with adsorbates (56). Details of the component interaction in binary metal particles are important in the final, catalytic output. In the case of Pt or Pd binary co-catalysts, several works showed different behaviour in the photocatalytic production of hydrogen for the same binary composition having core-shell or true alloying structures (57,58). In summary, considering the Pt co-catalyst, Pd addition not only will decrease the cost production but also would render a binary system with scientific interest as well as potentially improved photocatalytic properties.

In this contribution we studied a series of PtPd bimetallic materials supported in a high surface area Nb-doped titania support prepared using a microwave method followed by a spray drying and calcination process (59,60). The modified titania support with a 3 mol. % of Nb is particularly suited for achieving optimum activity under both UV and visible light illumination (23,51), opening the door for a fruitful use of sunlight as the energy source of the reaction. Here we presented a complete series of mono and bimetallic Pt-Pd co-catalysts and analyzed their performance in methanol photo-reforming under both UV and Visible light excitation. To compare the results in quantitative basis we measure hydrogen photo-production rates but also carried out the calculation of the true quantum efficiency under all illumination conditions. The latter is calculated according to the IUPAC guidelines and required; i) the full analysis of the optical properties of the catalysts at the liquid reaction medium, as well as ii) the modeling of the light-matter interaction at the reactor where catalytic measurements are carried out (61). This is here combined with a characterization of the materials using X-

ray diffraction, X-ray photoelectron, and optical (UV-visible and photoluminescence) spectroscopies, porosimetry, microscopy, as well as the in-situ study of the solids under reaction conditions using infrared spectroscopy.

2. Material and methods

2.1. Preparation and chemical composition of catalysts

Catalysts preparation was carried out in a propylene vial containing a mixture of 46.5 wt% of ethanol (industrial grade), 8.3 wt% of titanium butoxide (Aldrich, 97.00 %), certain amount of ammonium niobate (V) oxalate hydrate (3 mol.% of Niobium in cationic basis of the final TiO_2 support composition; Aldrich, 99.99%), and 55.3 wt.% of deionized water. The mixture was transferred and heated at 160 °C for 2 min under microwave irradiation by using a microwave reactor (Anton Paar, model Synthos 3000). The suspension obtained from de microwave reactor was atomized through a 2 mm nozzle in a YAMATO spray dryer (model DL410), at 2 bars and 200 °C. After drying, each sample received a thermal treatment at 500 °C in air during 2 h. A TiO_2 reference was also obtained and calcined following the above described procedure in absence of niobium.

The co-catalysts were introduced by a deposition method using H_2PtCl_6 (Aldrich) and $PdNO_3$ (Aldrich) solution. First, the sample was suspended by stirring in a deionized water solution for 30 minutes. After that, the proper quantity of H_2PtCl_6 or $PdNO_3$ was added to the solution (to get throughout the series a constant 0.4 mol. % of M = Pt and/or Pd on metal basis) and kept on stirring along 5 minutes more. This loading corresponds to a 1/0.55 wt. % in the case of Pt/Pd in the monometallic systems. The reduction was carried out using a $NaBH_4$ (Aldrich) aqueous solution (M/$NaBH_4$ molar ratio 1/5). The final solid was profusely rinsed with deionized water, collected by centrifugation and dried at 80 ^{0}C. The nomenclature used to identify the materials is: 3NbTi for the support, 3NbTi/Pt, 3NbTi/Pd, or 3NbTi/PtPd(x,y) where (x,y) is the Pt:Pd atomic ratio for the corresponding catalysts. A 1:1 Pt:Pd ratio was also deposited on the TiO_2 reference (sample Ti/Pt-Pd(1:1)). Chemical analysis (measured using atomic emission with inductive coupled plasma (ICP-AES) using an Optima 3300DV Perkin Elmer spectrometer) provided a metal concentration of 0.4 mol. % for all co-catalysts. Overall metal content is equal to the formal one within an error of 4.5 % for all samples.

2.2 Characterization of catalysts

XRD profiles of the samples were obtained using a Policristal X´Pert Pro PANalytical diffractometer using Ni-filtered Cu Kα radiation with a 0.02° step. The particle sizes were estimated using the Scherrer formalism (62). The BET surface areas were measured by nitrogen physisorption (Micromeritics ASAP 2010). UV−vis diffuse-reflectance spectroscopy experiments were performed on a Shimadzu UV2100 apparatus using Teflon as a reference and the results presented as Kubelka-Munk transform (63). Photoluminescence spectra were measured at room temperature on a Fluorescence Spectrophotometer (Perkin Elmer LS50B). Transmission electron microscopy (HTEM) and X-ray energy dispersive spectra (XEDS) were recorded on a JEOL 2100F TEM/STEM microscope. Particle size distributions of the noble metal were obtained counting more than 150 particles in all cases.

XPS data were recorded on 4 × 4 mm^2 pellets, 0.5 mm thick, prepared by slightly pressing the powered materials which were outgassed in the prechamber of the instrument at room temperature up to a pressure $<2 \times 10^{-8}$ Torr remove chemisorbed water from their surfaces. The SPECS spectrometer main chamber, working at a pressure $<10^{-9}$ Torr, was equipped with a PHOIBOS 150 multichannel hemispherical electron analyzer with a dual X-ray source working with Ag Kα ($h\nu$ = 1486.2 eV) at 120 W, 20 mA using C 1*s* as energy reference for adventitious carbon (284.6 eV). Surface chemical compositions were estimated from XP-spectra, by calculating the integral of each peak after subtraction of the "S-shaped" Shirley-type background (64) using the appropriate experimental sensitivity factors and the CASA-XPS (version 2.3.15) software. For the study of the Pt 4*f* signal of the Pt-containing solids, the background at the Pt 4*f* region of the titania support (Ti *3s* plasmon loss) was subtracted.

Diffuse Reflectance Infrared Fourier Transform Spectra (DRIFTS) were taken in a Bruker Vertex 80 FTIR spectrometer using a MCT detector and running under OPUS/IR software. The set-up consists of a praying mantis DRIFTS accessory (Harrick Scientific) and a reaction cell (HVC, Harrick Scientific). The reaction mixture was prepared by injecting 3000 ppm of methanol (≥99%; Aldrich) into a wet (3:7 methanol, MeOH, to water ratio) N_2 flow before entering the DRIFTS cell. Higher quantities of methanol provide a strong gas-phase IR signal which does not allow to obtain any information of the surface species. The DRIFTS spectra were collected in the range of 4000–600 $cm^{-1}$with a resolution of 2 cm^{-1}, by averaging 10 scans over a total of 1.2 seconds. In DRIFTS experiments in-situ light excitation was carried out using 365 nm

(20 nm half-width) radiation. Each sample, without any previous treatment, was subjected in a continuous mode (without modifying gas mixture) to a single, multi-step experiment which aims to test the: *i)* adsorption of the reactive mixture under dark conditions, *ii)* reaction mixture evolution under illumination conditions, and *iii)* subsequent stay at dark conditions. Spectra were taken after different exposure times to verify any evolution behavior.

2.3 Description of the reactor

Regarding photocatalytic measurements at liquid medium, they were carried out using a batch pyrex (cutting absorption edge at ca. 300 nm) reactor as depicted in Figure S1 of the Supporting Information section. The reactor contains a x:y (x:y going from 2:8 to 8:2 v/v) CH_3OH/H_2O mixture medium maintained at a constant temperature (20 ± 1 ^{0}C). The catalyst suspension (previously optimized at a 0.5 g L^{-1} concentration) was first degassed with an Ar stream for around 20 min. Subsequently, the Ar flow was settled down to 10 mL min^{-1} and stabilized before reaction. Ar is used as carrier to displace reaction gases from the reactor to the detection system. The solution inside a reactor was irradiated using a Hg-Xe lamp (500 W) and dichroic filters (LOT Quantum Design) allowing exposure of the catalysis to the UV (280-400 nm) or Visible (420-680 nm) wavelength range. The reaction rates for hydrogen production were evaluated at 3 hours from the start of the irradiation, where a pseudo-stationary situation is reached. The hydrogen rate was analyzed using an on-line Mass spectrometry (Onmistart 300).

2.4 Calculation of quantum efficiency

Quantum efficiency is defined, according to the IUPAC recommendation (61), as the ratio of the number of molecules reacting by the number of photon interacting with the sample (Equation 1).

$$\eta_q(\%) = 100 \times \frac{2 \times r\ (\text{mol m}^{-3}\text{s}^{-1})}{<e^a>\ (\text{Einstein m}^{-3}\text{s}^{-1})} \qquad 1$$

This equation takes into account that the transfer of two electrons are required to reduce two protons and thus to produce one H_2 molecule. The reaction rate of hydrogen production (r in equation 1) is measured in the liquid phase reactors as detailed in the previous subsection. To determine the denominator, we obtain the solution of the radiative transfer equation (RTE) in the heterogeneous reactor (65). As detailed in the

supporting information section, this renders the so-called local volumetric rate of photon absorption; e^a. In equation 1 we used the volume average values of the e^a observable parameter. The RTE (equation 2) measures the variation of intensity (associated to a beam of x-rays at wavelength λ in the direction of a solid angle vector , $\underline{\Omega}$) through a direction of the space (s).

$$\frac{dI_{\lambda,\underline{\Omega}}(\underline{x})}{ds} = -\kappa_\lambda I_{\lambda,\underline{\Omega}}(\underline{x}) - \sigma_\lambda I_{\lambda,\underline{\Omega}}(\underline{x}) + \frac{\sigma_\lambda}{4\pi}\int_{\Omega'=4\pi} p(\underline{\Omega}' \to \underline{\Omega})\, I_{\lambda,\underline{\Omega}'} d\underline{\Omega} \qquad 2$$

Where κ_λ is the absorption coefficient; σ_λ is the dispersion coefficient; and $p(\underline{\Omega}' \to \underline{\Omega})$ is the scattering phase measured with the Henyey and Greenstein phase function, as usually carried out for titania samples (66). These equations assume; (i) the emission radiation is negligible (at room temperature), and (ii) steady state condition during the photocatalytic processes. We included a summary of the mathematical procedure to calculate the denominator of equation 1 in the supporting information section.

3. Results and Discussion

3.1. Characterization results

XRD patterns for the samples under study are displayed in Figure 1. The patterns are dominated by the presence of the anatase polymorph profile (PDF 21-1272; space group $I4_1/amd$). A small quantity of rutile (PDF 21-1276; space group $P4_2/mnm$) can be also detected. A constant rutile concentration in the order of 5 % is observed throughout the sample series. The anatase primary particle size is constant within experimental error, being 13.1 ± 0.1 nm for all samples. Similar information about the rutile phase is not available due to its small concentration and the ill definition of the phase peaks in the corresponding XRD pattern(s). The influence of Nb incorporation to the titania matrix is analyzed by comparison with the pure titania reference pattern (Figure S3). As previously reported, Nb decreases the primary particle size of the anatase component with less significant changes in other (cell parameters; volume and tetragonallity) parameters (23). Absence of XRD noble metal signals can be noticed, in accordance of the relatively limited amount of active metal present in the catalysts. The structural similitude among our samples, more precisely in the support structural characteristics, extracted from the XRD analysis is additionally supported from the point of view of the surface area. BET values included in Table 1 only show a relatively mild decrease in

presence of the noble metals, indicating a possible limited occlusion of the pores of the support by presence of the co-catalyst. In any case this would only account for a modest decrease of the surface area of 3 to 6 m^2g^{-1}.

To obtain information on the noble metal (and oxide-titania) component(s) a microscopy study of the materials was carried out. Figure 2 (and Figure S4) displays representative TEM micrographs of selected noble metal containing samples. The TEM micrographs are dominated by ca. 10-15 nm particles of the titania component over which small, round-shaped (mostly spherical) metallic particles are clearly visible. The EDX results for the whole area presented in the right-hand side micrographs of Figure 2 are displayed in Figure S5. They evidence the presence of platinum and niobium in all samples. The metallic entities are marked with white arrows in the TEM micrographs. The face cubic centered (fcc) structure of such metallic entities is confirmed by the electron diffraction (ED) patterns presented as insets in Figure 2. Unfortunately, due to the limited differences in Pt and Pd bonding distances (fcc lattice constant of, respectively, 3.92 and 3.89 Å) electron diffraction can not distinguish between these two metals (or the possible alloying phases) in the bimetallic containing systems. The particle size histograms obtaining from TEM micrographs are included in Figure 3 for monometallic Pt and Pd, and bimetallic Pt-Pd (1:1) containing samples. While in all cases we detect rather small particles, some differences between samples are obvious. For a quantitative analysis, the corresponding particle size distributions are studied through their moments as summarized in Table 2. All samples display rather small mean values, of ca. 1.4/1.6 nm for monometallic samples and 1.7 nm for the bimetallic catalysts. Relatively limited differences appeared in the high order moments. Worth to note is that the skewness values indicate differences in the tailing, with Pt and Pt-Pd (1:1) concentrating the mass distribution at the opposite side than Pd. Still such differences are modest and particularly would be of limited significance in the reaction. To demonstrate this point, we calculated the average dispersion of the materials using the whole particle size distributions and assuming (as TEM suggest) quasi-spherical morphology (67). Values presented in Table 2 indicate the almost equal values for the monometallic samples (0.76-0.77) and a mild decrease for the Pt-Pd (1:1) sample (0.70). These values proof that the metallic surface area available for reaction suffers a relatively small variation within the sample series, being in any case smaller for bimetallic catalysts.

The chemical state of the noble metal component and the oxide cations was studied with XPS. Constant values of 458.2 ± 0.1 (Ti $2p_{3/2}$) and 209.3 ± 0.1 (Nb $3d_{5/2}$) eV for all samples analyzed are obtained (results not shown). These values correspond to Ti(IV) and Nb(V) oxidation states (68), as may be expected. Nb appears homogeneously distributed in the materials with absence of significant differences between bulk and surface concentrations according to the Nb/Ti ratio presented in Table 3.

The noble metal loading and the high dispersion of the Pt metal (according to the TEM measured dispersion; Table 2) complicate the obtaining of clean Pt *4f* XPS signals. Moreover, the Pt *4f* core level signal is overlapping with the Ti *3s* plasmon loss signal, a fact that increases the complexity of the analysis (68). Still, Figure 4 provides useful information about the Pt component. Although the signal to noise ratio (roughly 3 for monometallic Pt, ca. 2 for bimetallic Pt-Pd (1:1) and near absence of signal for Pd-rich bimetallic catalysts) precludes a good fitting analysis or even the shape analysis of the XPS spectra, the Pt *4f* contribution displays a maximum at ca. 71.4 eV for all samples. As bulk metallic Pt has a *4f* characteristic binding energy at 70.8 eV (17,68,69), a metallic state would be dominant for all samples. Small differences with the reference are ascribed to the particle size (ca. 1.5 nm) modulating metallic type states by quantum confinement. The zero valent chemical state of the noble metal is, in any case, in line with previous reports studying platinum deposition on titania where an inert atmosphere was utilized (70). The Pt *4f* XPS spectra for post-reaction specimens (see Figure 5 of the supporting information) suggest a limited evolution of Pt although, as mentioned, the signal to noise ratio does not allow to provide a quantitative analysis.

Pd signal is much better defined as judged by the spectra collected in Figures 6 and 7. This could be mainly due to the fact that is free of interferences with other (more intense) XPS peaks. According to Figure 6 monometallic Pd presents a $3d_{5/2}$ binding energy of 335.2 eV, intermediate between oxidized and reduced metallic states although approaching to the zerovalent one (68,71). The 3NbTi/Pt-Pd (x:y) samples show a consistent shift to lower binding energies. As larger the Pt content of the material as larger is the binding energy shift (Figure 6). A consistent low energy decrease in the Pd 3d binding energy has been previously ascribed to the formation of PtPd alloy particles (71). On the other hand, the relatively small effect of strain in core-shell structures typically produces the opposite trend of the Pd XPS peak, displaying a modest shift to higher binding energy (72). Therefore, the data indicate the more easy formation of PtPd alloy particles as higher is the Pt:Pd ratio. The single XPS component indicates

that the alloy particles (when formed) would have an average Pt:Pd atomic composition close to that measured by ICP-AES (Table 3). The co-deposition method is thus able to favor the interaction between the two noble metals but shows a clear dependence of the co-catalyst chemical nature (or, in other words, the Pt:Pd atomic ratio).

Interestingly, the variation of the Pd/Ti ratio measured by XPS through the bimetallic samples (Table 3) indicates that the surface of the PtPd particles suffers evolution under reaction conditions. This involves two distinct physical phenomena. First, in presence of Pt, the oxidized Pd(II) fraction increases with Pd content of the bimetallic co-catalyst after reaction. This triggers the second consequence, as the Pd oxidation process withdraws some Pd from the binary alloy in binary samples. This is reflected in the rather similar binding energies detected for the binary PtPd phase in post-reaction samples having Pt:Pd ratios equal or below 1. Unfortunately the low Pd content for samples having Pt:Pd ratios above one can not allow to extract information from XPS, see Figure 6. In any case, the similar binding energy detected for PtPd alloys in Figure 7 would be a consequence of their relatively close overall chemical composition (considering the oxidized Pd fraction, a Pt:Pd ratio of ca. 1:0.5 and 1:0.7 can be estimated for, respectively, the 3NbTi/Pt-Pd (1:1) and 3NbTi/Pt-Pd (1:2) samples after reaction) together with the effect of a composition gradient with produces a Pt enrichment at the surface. The combined effect makes the surface of the zerovalent binary noble metal particles (of the 3NbTi supported samples with Pt:Pd $\geq$ 1) essentially indistinguishable by XPS.

XPS was also utilized to compare the state of Pt and Pd in presence or absence of Nb at the support. Figures S6 and S7 present, respectively, Pt *4f* and Pd *3d* XPS spectra for the 3NbTi/Pt-Pd (1:1) and Ti/Pt-Pd (1:1) samples. Measurable differences between the co-catalyst(s) of these two samples concern the Pd peaks. Concretely, the bare titania material shows a significant increase in the oxidized Pd(II) contribution (Table 3). Also, the evolution under reaction is less pronounced in absence of Nb. Importantly, the zerovalent component of the post-reaction specimen shows a ca. 0.4 eV higher binding energy for the one of the Ti/Pt-Pd (1:1) sample, indicating the lower interaction (of Pd) with Pt in this case. Note thus that the comparative XPS study provides evidence of a strong influence of Nb in the (degree of) interaction between metals at the initial state as well as the evolution of the noble metal component under reaction conditions.

The samples show on the other hand relatively similar UV spectra, as shown in Figure 8. The characteristic intensity decay near 350-400 nm and ascribable to the titania band

gap dominates the spectra presented in Figure 8. Considering that the dominant (according to XRD) anatase phase is an indirect gap semiconductor (73), values of the corresponding band gap energy were calculated and included in Table 1. For the 3NbTi reference the band gap takes a value of 3.14 eV while for the samples it is essentially constant having a value of $3.08_5 \pm 0.01_5$ eV for all samples. This corresponds to a band gap dominated, as mentioned, by the major anatase phase. The band gap seems to suffer a small decrease upon Pt (Pd) deposition but a constant value is obtained for all samples after this preparation step (metal deposition). Note that the difference between the bare support and the monometallic Pt reference is within experimental error.

The noble metal component is not detected by any signal or contribution to the UV-visible spectra as the surface plasmon resonances in Pt and Pd cases do not usually render discrete peaks in the UV-visible spectrum due to the damping effect caused by d-d intraband transitions (1,3). Note that Pd optical properties are strongly size and shape dependent. This has been previously ascribed to variation in the absorption coefficient (74). The interaction of Pt and Pd with the titania support also can alter the UV-visible spectrum intensity by effect of plasmonic-like resonant energy transfer (75,76). The noble metal – titania interaction would facilitate the decay of hot electrons in electron – hole pairs, favoring separation of charge (77). Instead of a defined resonance, here we observed a broad tail (from ca. 400 to 550 nm) characteristic of Nb-doped materials and caused by the defects present at the anatase structure as a results of the charge compensation process originated by the doping process or, more precisely, the difference between the Nb (+5) and Ti (+4) oxidation states detected by XPS (78). The fraction of defects located at the surface seems to interact with the noble metals and modify the optical properties of the catalysts, presenting large absorption capability than the bare support in the visible range. Such an effect seems more important in the Pt-Pd bimetallic system. As mentioned, this behavior in the visible region of the optical spectra has been previously described in noble metal – titania systems (75-77).

The characterization results thus indicate an essentially unperturbed 3NbTi support throughout the sample series and likely the formation of bimetallic alloy particles in the initial state. Rather small mono and bimetallic particles are obtained having average sizes of ca. 1.5 to 2 nm in all cases. Importantly, samples suffer evolution under reaction. The chemical composition of the PtPd bimetallic particles is relatively similar in post-reaction specimens subjected to XPS analysis as a consequence of Pd depletion (and oxidation) from the initial metallic state and the enrichment of the surface in Pt. Nb

plays a critical role in limiting the degree of oxidation of Pd at the initial state and in the evolution of the bimetallic alloying particles under reaction conditions, facilitating the alloying between metals. The optical properties of the solids are rather similar in the UV range, presenting the (metal-containing) samples essentially equal band gap values, with some differences in the visible light region.

3.2. Photoactivity measurements: reaction rate and quantum efficiency observables

The photo-activity of the samples under UV and visible illumination is presented in Figure 9. The rather similar optical properties (illustrated in Figure S8 at the supporting information section) of the samples produces that the trends observed by the reaction rate or quantum efficiency variation through the series are rather similar. In fact, only small differences are detected in Figure 9 between the behavior of these two observables, the reaction rate and the efficiency, not affecting the trend but just the ratio between specific samples under visible illumination. So, the quantum efficiency changes shown in Figure 9 are dominated by variations in the reaction rate.

Marginal activity is presented by the support under all illumination conditions. The monometallic Pt and Pd samples display relatively similar values under UV illumination but Pd shows a value one order of magnitude inferior than the one displayed by the Pt containing sample under visible irradiation for both observables, the reaction rate and the quantum efficiency. Bimetallic samples display improved activity with respect to both Pt and Pd monometallic parent systems. An inverse volcano activity is presented by the activity through the series. Pt-rich bimetallic samples show clearly higher rates or efficiency values than Pd-rich ones, in agreement with previous experience for photocatalytic PtPd binary samples (52-55). Optimum activity is obtained for the 3NbTi/Pt-Pd (1:1) sample under all illumination conditions. The presence of Nb at the support is critical to render highly active materials as shown by the comparison with the Ti/Pt-Pd (1:1) reference (Figure 9). An important point is the rather high visible to UV ratio displayed by the 3NbTi/Pt-Pd (1:1) sample and, in general, by Pt-rich bimetallic samples. The (visible) quantum efficiency obtained for the former sample is more than 2 times higher than the one of the Ti/Pt-Pd (1:1) reference and more than 10 times of those of the monometallic references. Such figures indicate that Nb (either by affecting the physico-chemical characteristics of the alloy PtPd phase and or by direct interaction with the metals, this last point as suggested by the optical characterization) triggers an

enhancement of activity under visible illumination and thus a more fruitful use of sunlight for hydrogen photo-production.

For the 3NbTi/Pt-Pd (1:1) sample, Figure 10 illustrates the catalytic behavior as a function of the methanol to water ratio. The sample shows a relatively small sensitivity to such ratio, presenting high activity in the whole range of compositions explored. An increasing activity is observed nevertheless with the growth of the methanol to water ratio in the case of visible illumination. Maximum quantum efficiency values obtained are ca. 2.9 and 1.2 for, respectively, UV and visible light illumination. The stability of the sample photo-activity versus the liquid phase composition is noteworthy, as usually Pt-TiO_2 samples display low activity either at low or high ratios (17,23,79,80). The 3NbTi/Pt-Pd (1:1) sample has also very stable activity under prolonged exposure to the liquid phase reactant mixture. Figure S9 displays the rather stable activity presented by the 3NbTi/Pt-Pd (1:1) sample under continuous and cycling conditions, rendering similar activity under both conditions. The system reaches a pseudo-stationary state at ca. 3 h with no significant changes over all tested times on stream.

To summarize, the 3NbTi/Pt-Pd (1:1) sample shows (quantum efficiency) enhancement ratios of ca. 1.5 (1.5) and 11.5 (ca. 267) times under, respectively, UV and visible illumination with respect to the Pt (and Pd) monometallic references. It is interesting to note the large enhancement ratios obtained under visible illumination, indicating the suitability of the bimetallic formulation for sunlight operating conditions. As discussed previously the optical and charge handling effects related to the interaction of the noble metal and titania would be strongly promoted by Nb presence and the binary PtPd phases. We hypothesize (see below) that this phenomenon affects positively the activity of the binary co-catalyst samples. For a AM1.5 solar spectrum standard, the measurement of the efficiency presented in Figures 9 and 10 allows to estimate for sunlight (a similar derivation as above based on reaction rates or apparent quantum efficiencies values would not be possible) a maximum quantum efficiency of ca. 1.4 %, competitive with the few reports displayed in the literature for Pt-based materials under sunlight illumination (81).

3.3. Interpretation of quantum efficiency

In order to investigate the causes of the activity promotion in the case of the bimetallic samples we analyzed the physico-chemical properties of the post-reaction samples. This was carried out together with an analysis of the charge recombination with the help of

photoluminescence spectroscopy as well as an in-situ study of the materials under reaction conditions using infrared spectroscopy.

The 3NbTi support is stable under reaction conditions as judged by the surface area and band gap values included in Table 1 for post-reaction specimens of all monometallic and bimetallic samples. Essentially, absence of variation in both observables between fresh and post-reaction specimens can be noted in the values included in Table 1. The noble metal bimetallic entities however evolved under reaction conditions. The PdPt alloy particles present in bimetallic samples suffer an oxidation process of the Pd component under reaction conditions, as can be observed in the fitting results presented in Figure 7 for the 3NbTi/Pt-Pd (1:1) sample. The $3d_{5/2}$ XPS component above 336 eV is characteristic of PdO (68). This oxidation also occurs in the monometallic 3NbTi/Pd reference but in the case of the bimetallic sample, the zerovalent state appears at a binding energy shifted to lower values with respect to both the initial 3NbTi/Pt-Pd (x:y) state(s) and the Pd pre and post-reaction specimens. According to the previous discussion of the XPS results, this fact indicates that some Pd is (partially) separated by oxidation of the PtPd alloy particles and concomitantly generates an enrichment in Pt at the binary entities, which is detected by a decreasing Pd $3d_{5/2}$ binding energy (between fresh and used samples) for the zerovalent phase (71,72). The specific alloying phase generated under reaction conditions would be, as pointed out in the literature, a Pt-rich alloy, beneficial for photo-activity when compared with monometallic samples (52-55). The XPS results provide evidence of a few trends along the samples of the series. First, as lower the Pd content of the binary co-catalyst at the initial state as larger the interaction with Pt (Figure 6). Second, under reaction conditions and considering Pt:Pd ratios equal or below 1, as lower the Pd content is in the composite co-catalyst sample, as lower the oxidized Pd fraction (which appears detrimental for activity) appears (Figure 7; Table 3). Pt-rich binary co-catalyst compositions (which are also Pt-enriched at surface under reaction conditions) favor an effective interaction between the two noble metals with direct consequences in activity. The optimum activity within Pt-rich binary samples would appear for the Pt:Pd ratio which provides maximum (number of) binary interaction(s) between the two metals.

The physical origin of the photo-activity in the binary co-catalyst samples is first analyzed in terms of the charge handling properties using photoluminescence. Figure 11 displays photoluminescence profiles of the samples under UV (365 nm) excitation while Figure 12 does the same but under visible (425 nm) illumination. Excitation under UV

shows the typical photoluminescence spectra of the reference sample, the bare support oxide. Such spectrum is composed in fact by two types of transitions (which centers at ca. 450 and around 500-550 nm) corresponding to the annihilation of conduction band free electrons with trapped holes and valence band free holes with trapped electrons (82,83). Mono and bimetallic samples show the same profile than the support reference but having differences in the overall intensity. A lower intensity is indicative of a lower charge recombination and thus would suggest a better charge handling properties for the corresponding solid, with beneficial consequences in the photo-activity. The optimum charge handling properties seems to correspond to the 3NbTi/Pt-Pd (2:1) sample, having an alloy composition similar to the most active sample after reaction. The photoluminescence spectra under visible (425 nm) illumination are displayed in Figure 12 and show the typical relatively weak signals associated to defect state(s) de-excitation over a decay curve corresponding to the excitation line (82,83,84). In this case, differences among samples are rather limited and would not justify any photo-catalytic differences among the solids of the series. So, the above discussion stresses that the metal – support interface can play in photocatalysis. Under UV this can be directly linked to charge handling and recombination decrease while the effect under visible illumination seems mostly related to enhancement of the optical absorption as well as local effects which may affect charge transfer between the components and may influence the activity of surface sites located at the interface (74-77).

To further progress in the interpretation of the photo-activity Figures 13 to 15 show infrared results corresponding to Pt and Pd monometallic samples and the 3NbTi/Pt-Pd (1:1) sample. These figures display results under UV illumination conditions and contain plots concerning difference spectra taking as background the first spectrum recorded during each step (from *i* to *iii*) of the treatment of the samples consisting in a sequential: *i)* adsorption of methanol in presence of water vapour, *ii)* reaction mixture (methanol:water) under illumination conditions, and *iii)* subsequent stay at dark conditions under the same reactive mixture used in previous steps of the experiment. Samples were pre-treated only with a nitrogen flow (10 min) prior to IR measurements.

Adsorption of methanol prior to illumination generates surface methanol and methoxy species (lower row in Figures 13 to 15). In all cases studied, methanol (C-H contributions at 2948/2838 cm^{-1}) seems to have larger intensity than methoxy (2922/2820 cm^{-1}) species (17,85,86). This is concomitantly observed with a weak decrease of isolated hydroxyl of titania at ca. 3695 cm^{-1} as well as a more strong

decreasing of the water (and interacting hydroxyl radicals) signals at ca. 3650-3200 and 1640 cm^{-1} (Figures S10 and 13 to 15). C-O stretching bands for these two (methanol/methoxy) adsorbate species appear around 1033 cm^{-1} but the bands are so broad that cannot be easily resolved. Additional broad peaks in the ca. 1500-1100 cm^{-1} region are indicative of the formation of other species. However, their ill defined shapes and positions can not allow to obtain information relative to their chemical nature, being in any case carboxylates and or carbonates the dominant species contributing to the infrared signal(s) in this region (17,85,86).

Under reaction conditions the evolution of the methanol related species is evident in Figures 13 to 15 by the presence of negative signals in the C-H and C-O stretching regions. This would correspond to either desorption or consumption of the methanol by reaction. The presence of carbon dioxide (see signal at the 2330-2400 cm^{-1} ascribable to the gas phase molecule) indicates that reaction takes place in all cases studied. Differences among samples are consistent with the larger activity of the 3NbTi/Pt-Pd (1:1) sample with respect to the monometallic references (Figure 9). In addition, the intensity of the carbon dioxide infrared signal correlates well with the activity displayed in Figure 9. Only in the case of the 3NbTi/Pt-Pd (1:1) sample we observe the presence of additional IR signals. We detected a signal at ca. 2020 cm^{-1} likely associated with the on-top CO adsorption. Surface CO absorbed on an on-top mode on rather small Pt particles of near 1 nm give rise to a signal at the frequency mentioned (87,88). This again reinforces the idea that Pt would be preferentially located at the surface of the metallic particles. It is important to note that the characteristic CO species over titania (ca. 2175-2120 cm-1; see ref. 89) are not observed here nor for the support alone under reaction (result not shown). This analysis indicates that methanol-related fragments approaching the platinum support interface are quickly oxidized, forming carbon oxides, in contraposition to the slower reaction of carboxylate-type species at the bare titania surface.

The progressive variation of the CO signal under reaction (as we show difference spectra, indicative of CO evolution), the constancy of relatively weak CO signals at post-reaction, dark conditions (as we show difference spectra from the initial spectrum at dark, no significant CO increase can be discerned), and the (qualitatively inverse) correlation with the intensity of CO_2 molecule at gas phase suggest that the metal-TiO_2 interface plays an key role in activating the methanol molecule. Note that the process renders CO_2 as CO gas is absent at the gas phase (considering both IR and photo-

catalytic results) and presumably transformed at the noble metal surface in a fast step. The results are rationalized in terms of a water gas shift type reaction occurring exclusively at the metal-support interface and where the water or OH-related surface species of the oxide support react with carbon dioxide or more like carboxylate/carbonate surfaces species to generate CO and hydrogen. As mentioned, this happens only in the case of the bimetallic particles (Figures 13 to 15). This shows a pathway to activate the carbon containing molecules distinctive of the bimetallic samples in our series. A bifunctional mechanism with active contribution from the support and the bimetallic phases would be thus operative. The binary PtPd co-catalyst not only favors charge separation and takes care of the protons joining at the hydrogen molecule. It also has a clear role in handling carbon containing products through an active role at the metal-support interface.

4. Conclusions

In this work we analyzed the performance of bimetallic PtPd particles supported in Nb-doped TiO_2 in hydrogen photo-production using methanol as a sacrificial agent. Our systems are composed by a dominant anatase phase and noble metal particles. The co-catalyst noble metal particles present an average particle size between 1.4 to 1.7 nm. For fresh (before reaction) composite co-catalyst systems, the interaction between the two metals is favoured for Pt:Pd ratios equal or above 1. Under reaction Pd is partially oxidized in all mono and bimetallic catalysts but PtPd alloy particles are observed for all binary co-catalysts, having thus Pt-rich compositions. This shows that the co-deposition preparation method can provide an effective way to allow the intimate contact between the two metals on titania supported samples. For the 3NbTi/Pt-Pd (1:1) sample such particles have an average Pt:Pd chemical composition near to 2:1 under reaction conditions and, according to infrared results, maintain a dominant presence of Pt at the surface. Nb at the support is shown to play a role in triggering the initial (dominant) reduced state of the noble metal PtPd alloy particles as well as the controlling the way they evolve under reaction conditions, limiting the formation of oxidized Pd. Thus, noble metal(s) and Nb work cooperatively to shape the binary co-catalyst physico-chemical properties.

The binary PtPd co-catalysts display in all cases tested (initial Pt:Pd ratios from 2:1 to 1:2) an improved catalytic performance with respect to the monometallic references having essentially similar surface exposed to the reactive atmosphere (in fact a ca. 10 %

slight lower dispersion is detected in the initial stage of the 3NbTi/Pt-Pd (1:1) sample with respect to the monometallic reference materials). The measured quantum efficiency indicates that the 3NbTi/Pt-Pd (1:1) sample overperforms the monometallic Pt/Pd samples by a 1.5/1.5 factor under UV illumination and a 11.5/267 factor under visible illumination. High UV and visible light activity are obtained for all methanol:water mixtures tested with the 3NbTi/Pt-Pd (1:1) sample, a fact not shared by the monometallic Pt and Pd reference systems. High quantum efficiency for all methanol:water mixtures together with stable operation for extended time on stream prove the suitability of the PtPd bimetallic co-catalyst having alloy (surface Pt-enriched) PtPd particles for sunlight-operated processes. The interpretation of the photo-catalytic activity was conducted with the help of photoluminescence studies and an in-situ infrared analysis under reaction conditions. These tools provide evidence that the PtPd binary catalysts may facilitate the handling of charge carriers with respect to monometallic references but this does not seem a critical issue to justify the activity behavior through the series of samples, particularly under visible illumination. On the other hand, the in-situ infrared shows that limiting Pd oxidation with the parallel formation of Pt-rich surface, PtPd alloy particles together with the interaction of such alloy particles with the Nb-containing support drive to an efficient handling of methanol-derived surface moieties, boosting the production of hydrogen.

Acknowledgements

We are thankful to MINECO (Spain) for supporting the work carried out through the ENE2016-77798-C4-1-R grant and the Secretaria de Ciencia Tecnologia e Innovacion of CDMX (SECITI, Mexico).

Supporting Information

Data concerning TEM, XEDS, in-situ infrared measurements and optical properties of the samples, together with numerical procedures used for calculation of the true quantum efficiency parameter are presented in the supporting information section

References

1 X. Chen, S. Shen, L. Guo, S.S. Mao, Chem. Rev., 110 (2010) 6503-6570.
2 K. Maeda, K. Domen, J. Phys. Chem. Lett., 1 (2010) 2655-2661.
3 A. Kubacka, M. Fernández-García, G. Colón, Chem. Rev., 112 (2012) 1555-1614.
4 Y. Ma, X. Wang, Y. Jia, X. Chen, H. Han, C. Li, Chem. Rev., 114 (2014) 9987-10043.
5 X. Li, J. Yu, J. Low, Y. Fang, J. Xiao, X. Chen, J. Mater. Chem. A, 3 (2015) 2485-2534.
6 T. Kawai, T. Sakata, Nature, 286 (1980) 474-476.
7 Y. Li, Y. Xie, S. Peng, G. Lu, S. Li, Chemosphere, 63 (2006) 1312-1318.
8 A. Patsoura, D.I. Kondarides, X.E. Verykios, Catal. Today, 124 (2007) 94-102.
9 X. Fu, J. Long, X. Wang, D.Y. Leung, Z. Ding, L. Wu, Z. Zhang, Z. Li, X. Fu, Int. J. Hydrog. Energy, 33 (2008) 6484-6491.
10 W. Sun, S. Zhang, Z. Liu, C. Wang, Z. Mao, Int. J. Hydrog. Energy, 33 (2008) 1112-1117.
11 M. Bowker, Catal. Lett., 142 (2012) 923-929.
12 Y. Ma, Q. Xu, X. Zong, D. Wang, G. Wu, X. Wang, C. Li, Energy Environ. Sci., 5 (2012) 6345-6351.
13 E. Pulido Melián, C.R. López, A.O. Méndez, O.G. Díaz, M.N. Suárez, J.D. Rodríguez, J. Navío, D.F. Hevia, Int. J. Hydrog. Energy, 38 (2013) 11737-11748.
14 D. Tristantini, M. Ibadurrohman, Int. J. Energy Res., 37 (2013) 1372-1381.
15 G.N. Nomikos, P. Panagiotopoulou, D.I. Kondarides, X.E. Verykios, Appl. Catal. B-Environ., 146 (2014) 249-257.
16 A. Kubacka, M. J. Munoz-Batista, M. Fernández-García, S. Obregón, G. Colón, Appl. Catal. B-Environ., 163 (2015) 214-222.
17 O. Fontelles-Carceller, M.J. Muñoz-Batista, E. Rodríguez-Castellón, J.C. Conesa, M. Fernández-García, A. Kubacka, J. Catal., 347 (2017) 157-169.
18 Y.-J. Yuan, J.-R. Tu, Z.-J. Ye, D.-Q. Chen, B. Hu, Y.-W. Huang, T.-T. Chen, D.-P. Cao, Z.-T. Yu, Z.-G. Zou, Appl. Catal. B-Environ., 188 (2016) 13-22.
19 J. Highfield, M. Chen, P. Nguyen, Z. Chen, Energy Environ. Sci., 2 (2009) 991-1002.
20 G.L. Chiarello, M.H. Aguirre, E. Selli, J. Catal., 273 (2010) 182-190.
21 T.A. Kandiel, I. Ivanova, D.W. Bahnemann, Energy Environ. Sci., 7 (2014) 1420-1425.
22 A. Naldoni, M. D'Arienzo, M. Altomare, M. Marelli, R. Scotti, F. Morazzoni, E. Selli, V. Dal Santo, Appl. Catal. B-Environ., 130 (2013) 239-248.
23 O. Fontelles-Carceller, M.J. Muñoz-Batista, J.C. Conesa, M. Fernández-García, A. Kubacka, Appl. Catal. B 216 (2017) 133-145.
24 C. Zhang, Y. Zhou, Y. Zhang, S. Zhao, J. Fang, X. Seng, New J. Chem. 41 (2017) 11089-11096.
25 G. Colón, Appl. Catal. A-Gen., 518 (2016) 48-59.
26 L. Sheppard, T. Bak, J. Nowotny, J. Phys. Chem. B, 110 (2006) 22447-22454.
27 W. Li, T. Bak, A. Atanacio, J. Nowotny, Appl. Catal. B-Environ., 198 (2016) 243-253.
28 W.J. Ong, L.L. Tan, S.P. Chai, S.T. Yong, A.R. Mohamed, ChemSusChem, 7 (2014) 690-719.

29 D. Wang, T. Hisatomi, T. Takata, C. Pan, M. Katayama, J. Kubota, K. Domen, Angew. Chem.-Int. Edit., 52 (2013) 11252-11256.
30 Y. Li, G. Lu, S. Li, Appl. Catal. A-Gen., 214 (2001) 179-185.
31 S. Yin, T. Sato, J. Photochem. Photobiol. A-Chem., 169 (2005) 89-94.
32 W.Y. Teoh, L. Mädler, R. Amal, J. Catal., 251 (2007) 271-280.
33 C.-H. Lin, J.-H. Chao, C.-H. Liu, J.-C. Chang, F.-C. Wang, Langmuir, 24 (2008) 9907-9915.
34 J.S. Jang, S.H. Choi, H.G. Kim, J.S. Lee, J. Phys. Chem. C, 112 (2008) 17200-17205.
35 M.A. Khan, M.S. Akhtar, S.I. Woo, O.-B. Yang, Catal. Commun., 10 (2008) 1-5.
36 H. Wang, Z. Wu, Y. Liu, Y. Wang, Chemosphere, 74 (2009) 773-778.
37 T. Sreethawong, C. Junbua, S. Chavadej, J. Power Sources, 190 (2009) 513-524.
38 J. Liu, G. Liu, M. Li, W. Shen, Z. Liu, J. Wang, J. Zhao, L. Jiang, Y. Song, Energy Environ. Sci., 3 (2010) 1503-1506.
39 S. Obregón, G. Colón, Appl. Catal. B-Environ., 144 (2014) 775-782.
40 Z.H. Al-Azri, W.-T. Chen, A. Chan, V. Jovic, T. Ina, H. Idriss, G.I. Waterhouse, J. Catal., 329 (2015) 355-367.
41 Y.H. Li, C. Peng, S. Yang, H.F. Wang, H.G. Yang, J. Catal., 330 (2015) 120-128.
42 Z. Jiang, Z. Zhang, W. Shangguan, M.A. Isaacs, L.J. Durndell, C.M. Parlett, A.F. Lee, Catal. Sci. Technol., 6 (2016) 81-88.
43 Z. Jian, S. Pang, T. Dittich, Y. Gao, W. Nie, J. Cui, R. Chen, H. An, F. Fan, C. Li, Nano Lett. 17 (2017) 6735-6741.
44 S. Trasatti, J. Electroanal. Chem., 39 (1972) 163-184.
45 M. Luo, P. Lu, W. Yao, C. Huang, Q. Xu, Q. Wu, Y. Kuwahara, H. Yamashita, ACS Appl. Mater. Interfaces, 8 (2016) 20667-20674.
46 Y. Mizukoshi, Y. Makise, T. Shuto, J. Hu, A. Tominaga, S. Shironita, S. Tanabe, Ultrason. Sonochem., 14 (2007) 387-392.
47 J.C. Colmenares, A. Magdziarz, M.A. Aramendia, A. Marinas, J.M. Marinas, F.J. Urbano, J.A. Navio, Catal. Commun., 16 (2011) 1-6.
48 M.-C. Wu, I.-C. Chang, W.-K. Huang, Y.-C. Tu, C.-P. Hsu, W.-F. Su, Thin Solid Films, 570 (2014) 371-375.
49 M. Bowker, C. Morton, J. Kennedy, H. Bahruji, J. Greves, W. Jones, P.R. Davies, C. Brookes, P. Wells, N. Dimitratos, J. Catal., 310 (2014) 10-15.
50 M. Bowker, H. Bahruji, J. Kennedy, W. Jones, G. Hartley, C. Morton, Catal. Lett., 145 (2015) 214-219.
51 U. Caudillo-Flores, M.J. Muñoz-Batista, J.A. Cortés, M. Fernández-García, A. Kubacka, Mol. Catal. 437 (2017) 1-10.
52 Y. Shiraishi, Y. Takeda, Y. Sugano, S. Ichikawa, S. Tanaka, T. Hirai, Chem. Commun., 47 (2011) 7863–7865.
53 O. Ressler, A. Louvet, V. Keller, N. Keller, Chem. Comm. 47 (2011) 531-533.
54 A. Zeilinska-Jurek, J. Hopte, Catal. Today 230 (2014) 282-287
55 M. Luo, P. Lu, W. Yao, C. huang, Q. Xu, Q. Wu, Y. Kuwahara, H. Yamashita, ACS Appl. Mater. Interfaces 8 (2016) 20667−20674.
56 Y. Yayama, T. Ishimoto, M. Hayama, J. Alloy Compds 653 (2015) 444-452.
57 A. Gallo, M. Marcelli, P. Psaro, V. Gombac, T. Montini, P. Fornasiero, P. Piero, V. Dal Santo, Green Chem. 14 (2012) 330-333.
58 Q. Yang, W. Jones, P.P. Wells, D. morgan, L. Dong, B. Hu, N. Dimitratos, M. Dong, M. Bowker, F. Besenbacher, R. Su, G. Hutchings, Appl. Catal. A 518 (2016) 213-220.

59 U. Caudillo-Flores, M.J. Muñoz-Batista, F. Ung-Medina, G. Alonso-Núñez, A. Kubacka, J.A. Cortés, M. Fernández-García, Chem. Eng. J., 299 (2016) 393-402.
60 M.J. Muñoz-Batista, U. Caudillo-Flores, F. Ung-Medina, M. del Carmen Chávez-Parga, J.A. Cortés, A. Kubacka, M. Fernández-García, Appl. Catal. B-Environ., 201 (2017) 400-410.
61 S.E. Braslavsky, A.M. Braun, A.E. Cassano, A.V. Emeline, M.I. Litter, L. Palmisano, V.N. Parmon, N. Serpone, Pure Appl. Chem., 83 (2011) 931-1014.
62 P. Scherrer,Göttinger Nachrichten Gesell., 2 (1918) 98-104.
63 P. Kubelka, J. Op. Soc. Am. 38 (1948) 448-457.
64 D.A. Shirley, Phys. Rev. B 5 (1972) 4709-4714
65 R.L Romero, O.M. Alfano, A.E. Cassano, Ind. Eng. Chem.. Res. 36 (1997) 3094-3109.
66 M.L. Satuf, R.J. Brandi, A.E. Cassano, O.M. Alfano, Ind. Eng. Chem. Res., 44 (2005) 6643-6649
67 A.Kubacka, A. Martínez-Arias, M. di Michel, M. Fernández-García, M.A. Newton, Journal of Catalysis 270 (2010) 275–284
68 C.D. Wagner, W.M. Riggs, L.E. Davis, J.F. Moulder, "Handbook of X-ray Photoemission spectra". Muilenber, G.E.; Ed. (Perkin-Elmer, Minnesota, 1976).
69 A.A.S. Karakoti, J.E.S. King, A. Vincet, S. Seal, Appl. Catal. A 388 (2010) 262-271.
70 Z. Wei, E. Kowalska, K. Wang, C. Colbeau-Justin, B. Ohtani, Catalysis Today 280 (2017) 29–36.
71 Y. Kim, Y. Noh, E.J. Lim, S. Lee, S.M. Choi, W.B. Kim, J. Mater. Chem. A 2 (2014) 6976-6987.
72 K. Hassan, A.S.M.I. Uddin, G.-S. Chung, Sensors Actuators B 234 (2017) 435-445.
73 M. Fernandez-Garcia, A. Martinez-Arias, J. Hanson, J. Rodriguez, Chem. Rev., 104 (2004) 4063-4104.
74 S. Cao, Y. Li, B. Zhu, J. Yu, ACS Sust. Chem. Eng. 6 (2018) 6478-6487.
75 X. Weing, C. Shao, X. Li, N. Lu, K. Wang, Z. Zhang, Y. Lin, Nanoscale 8 (2016) 11034-11043.
76 P. Zhang, C. Shao, Z. Zhang, M. zhang, J. Mu, Z. Guo, Y. Lin, Nanoscale 3 (2011) 3357-3363.
77 G.V Hartland, L.V. Besteiro, P. Johns, A.O. Hovorov, ACS Energ. Lett. 2 (2017) 1641-1653.
78 L. Kong, C. Wang, H. Zheng, X. Zhang, Y. Liu, J. Phys. Chem. C, 119 (2015) 16623-16632.
79 E. Pulido Melián, J. A. Ortega Méndez, D.E. Santiago, J.M. Doña Rodríguez, O. González Díaz, J. Photochem. Photobiol. A 312 (2015) 45-54.
80 G. Wua, T. Chen, W. Su, G. Zhou, X. Zong, Z. Lei, C. Li, G. Wu, Int. J. Hydr. Energy 33 (2008) 3841-3848.
81 J. Liu, Y. Liu, N. Liu, Y. Han, X. Zhang, H. Huang, Y. Lifshitz, S.-T. Lee, J. Zhong, Z. Kang, Z, Science 347 (2015) 970−974.
82 T. Tachikawa and T. Majima, J. Am. Chem. Soc., 131 (2009) 8485-8494.
83 C.C. Mercado, Z. Seeley, A. Bandyopadhyay, Z. Bose, J.L. McHale, ACS Applied Mater. Interf. 3 (2011) 228-235.
84 M.J. Muñoz-Batista, A. Kubacka, M. Fernández-García, Catal. Sci. Technol., 2014, 4, 2006-2015.
85 A. Yamakata, T-A Ishibashi, H. Onishi, J. Phys. Chem. B 106 (2002) 9122-9125.
86 P.A. Panatoyov, S.T. Burrows, J.P. Morris, J. Phys. Chem. C 116 (2012) 6623-6635.
87 P. Hollins, Surf. Sci. Rep. 16 (1992) 51-132.

88 L.M. Kustov, D. Ostgard and W.M.H. Sachtler, Catal. Lett. 9 (1991) 121-128.
89 L. Mino, G. Spoto, S. Bordiga, A. Zecchina, J. Phys. Chem. C 117 (2013) 11186–11196.

Table 1. Main physicochemical properties of the samples.[a]

Sample	Crystal size (Fresh/Used; nm)	BET surface area (Fresh/Used; $m^2 g^{-1}$)	Band gap (Fresh/Used; e^-V)
3NbTi	13.1/13.1	76.0_5/76.1	3.14/3.13
3NbTi/Pt	13.2/13.2	67.6/67.3	3.10/3.09
3NbTi/Pt-Pd (2:1)	13.1/13.1	72.2/72.1	3.07/3.05
3NbTi/Pt-Pd (1:1)	13.0/13.0	73.3/73.6	3.08/3.08
3NbTi/Pt-Pd (1:2)	13.1/13.1	74.3/74.1	3.09/3.08
3NbTi/Pd	13.0/13.1	70.0/70.1	3.08/3.06

a) Average standard error: Anatase crystal size: 0.06 nm; BET area: 2.2 $m^2 g^{-1}$; Band gap: 0.035 eV

Table 2. Average particle size (first raw order moment), variance (second raw order moment), higher normalized central moments, and dispersion of the noble metal particles detected by TEM in selected samples. See text for details.

Sample	Size (nm)	Variance (nm^2)	Skewness	Kurtuosis	Dispersion[a]
3NbTi/Pt	1.44	0.47	3.84	0.54	0.77
3NbTi/Pd	1.61	0.16	-0.31	-0.51	0.76
3NbTi/Pt-Pd (1:1)	1.72	0.31	0.84	0.39	0.70

a) Average standard error: 8.5 %.

Table 3. XPS and Chemical Analysis Pd/Ti and Nb/Ti atomic ratios. The Pd(II)/Pd(0) ratio from XPS is also included.[a]

Sample	Atomic ratio			
	Pd^{II}/Pd^{0}	Pd/Ti	Pd/Ti (ICP-AES)	Nb/Ti[b]
3NbTi	-	-	-	0.030
3NbTi/Pt	-	-	-	0.030
3NbTi/Pt-Pd (2:1)	n.d[c].	n.d.[c]	0.0012	0.030
3NbTi/Pt-Pd (1:1)	0	0.0023	0.0020	0.030
3NbTi/Pt-Pd (1:2)	0	0.0043	0.0027	0.030
3NbTi/Pd	0	0.0078	0.0041	0.030
3NbTi/Pt-Pd (1:1)-Post	0.51	0.0026	0.0021	0.030
3NbTi/Pt-Pd (1:2)-Post	0.63	0.0046	0.0027	0.030
3NbTi/Pd-Post	0.55	0.0072	0.0041	0.030
Ti/Pt-Pd (1:1)	1.21	0.0024	0.0020	0.030
Ti/Pt-Pd (1:1)-Post	0.80	0.0023	0.0020	0.030

a) Average standard error: Pd(II)/Pd(0) ratio 0.05;Pd/Ti 0.0012; Pd/Ti (AAS) 0.0002; Nb/Ti 0.0002.

b) XPS and Chemical analysis give equal values within error.

c) n.d. not determined; quantification not possible due to a weak signal

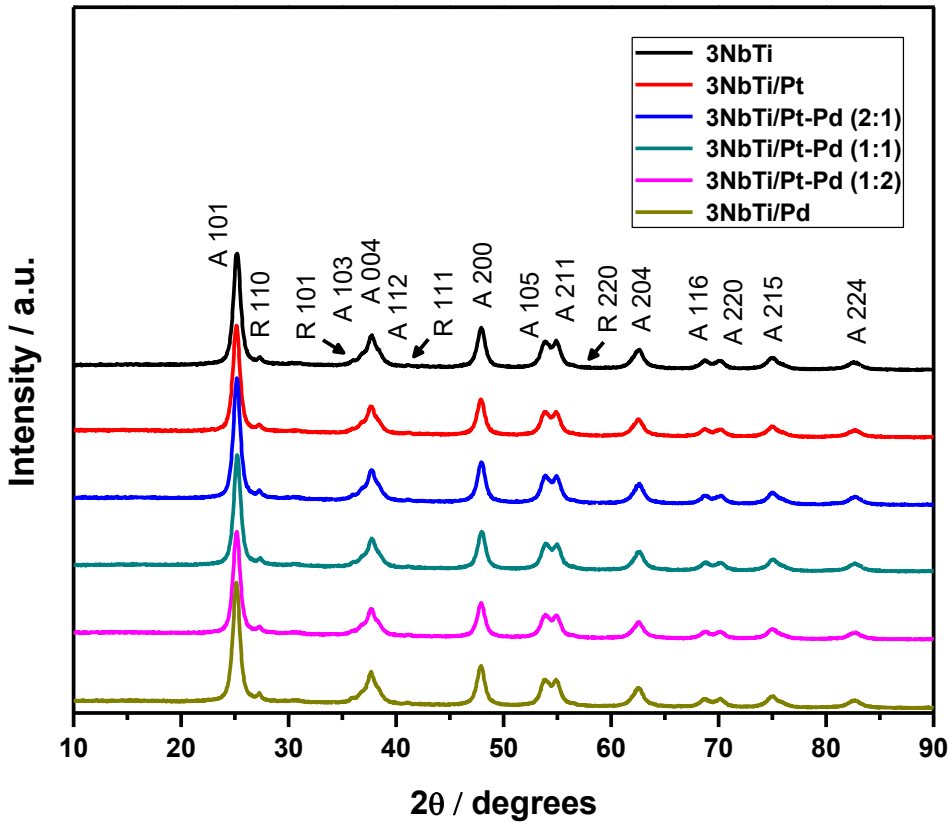

Figure 1. XRD patterns of the studied samples.

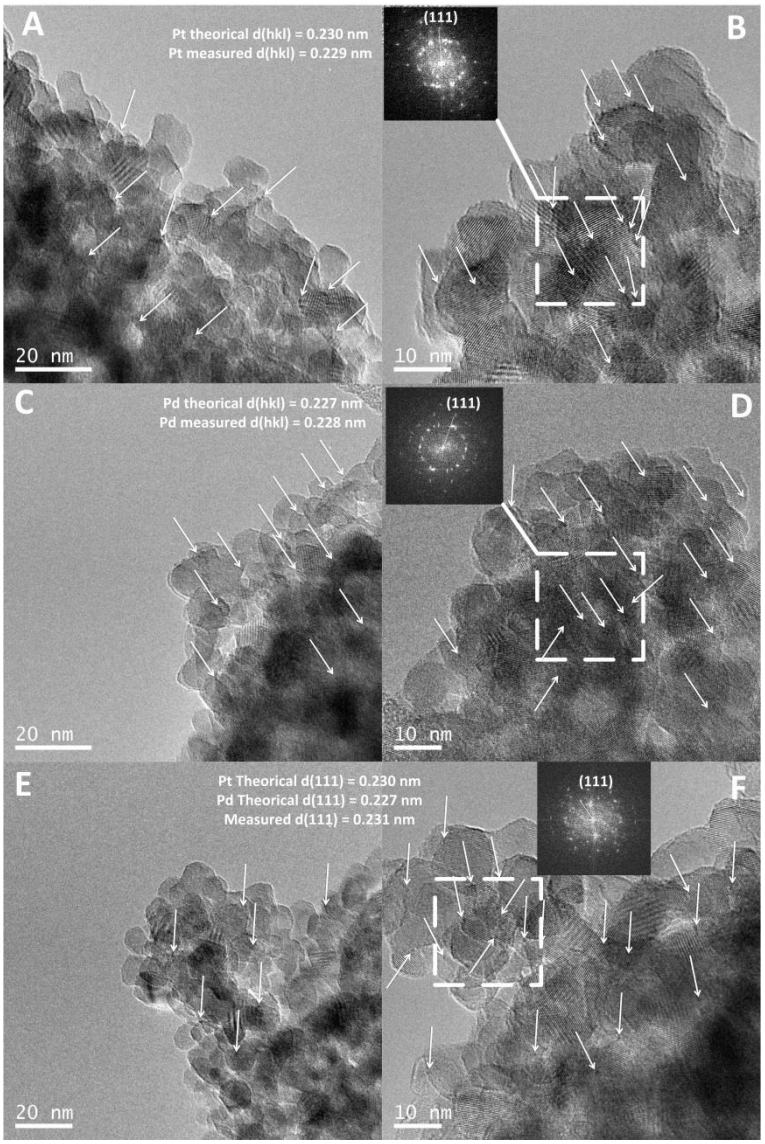

Figure 2. TEM images of the 3NbTi/Pt (A and B) , 3NbTi/Pd (C and D) and 3NbTi/Pt-Pd (1:1) catalysts (E and F). Arrows indicate the location of selected platinum, palladium or platinum-palladium nanoparticles. Inset: electron diffraction patterns obtained in areas delimitated by red squares.

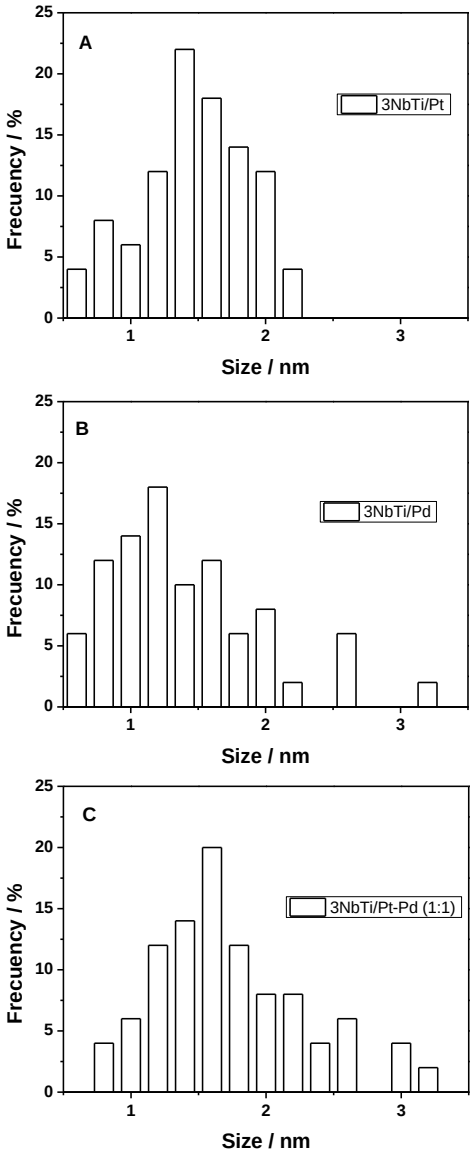

Figure 3. Distribution of particle size for selected samples as measured from TEM data.

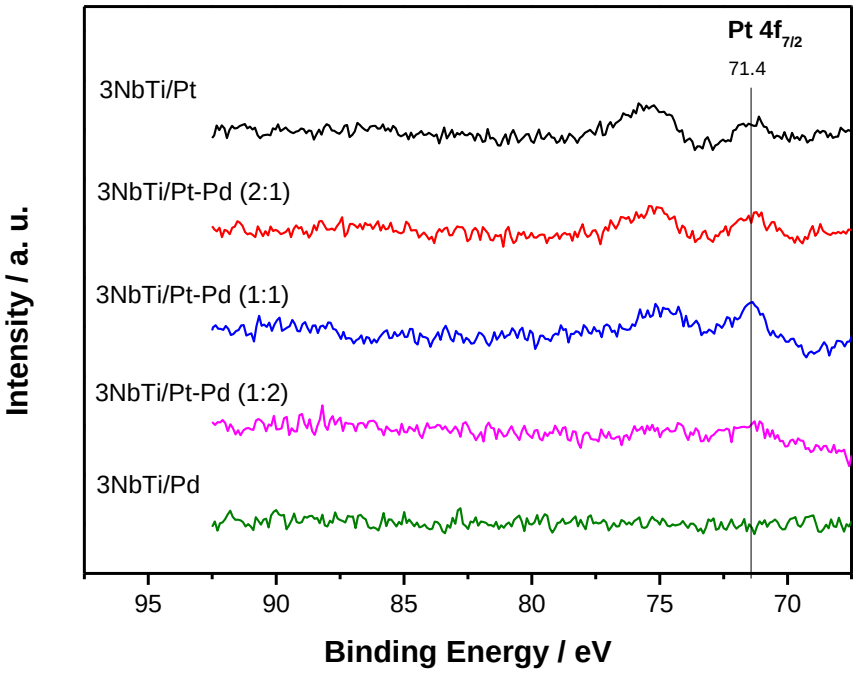

Figure 4. Pt *4f* XPS spectra for the studied samples.

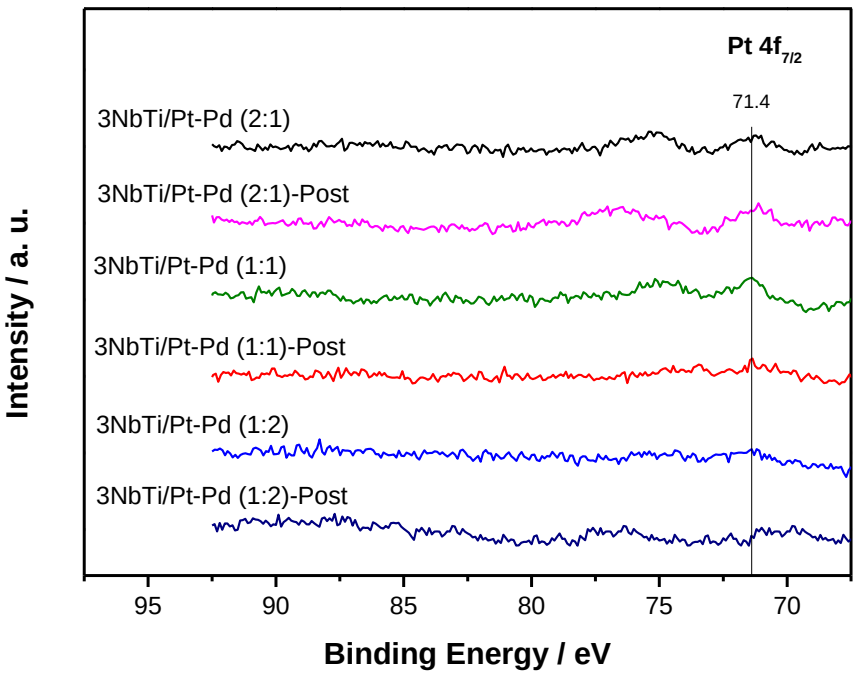

Figure 5. Pt *4f* XPS spectra for the Pt-Pd initial and post-reaction samples

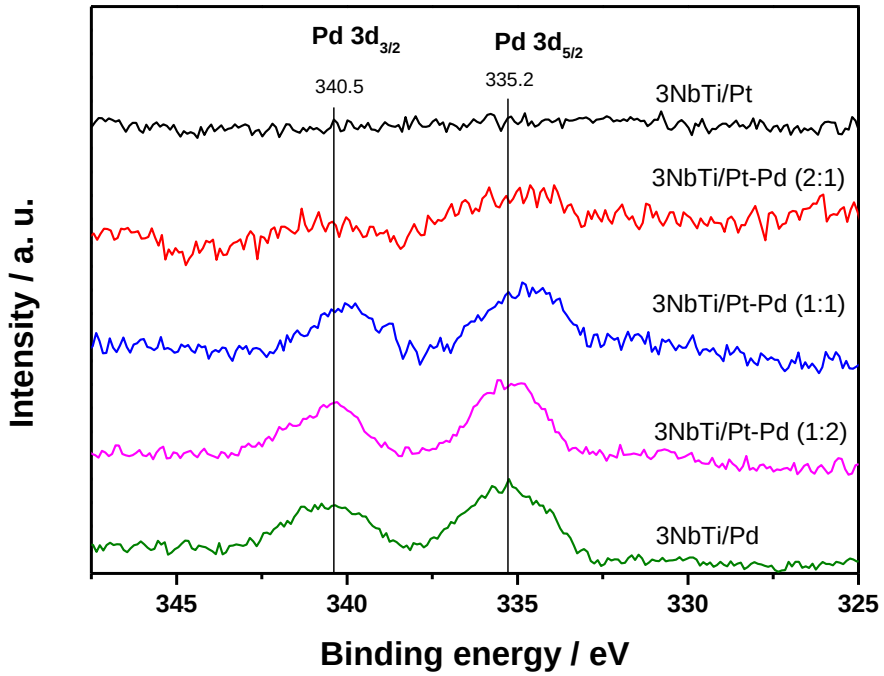

Figure 6. Pd *3d* XPS spectra for the studied samples.

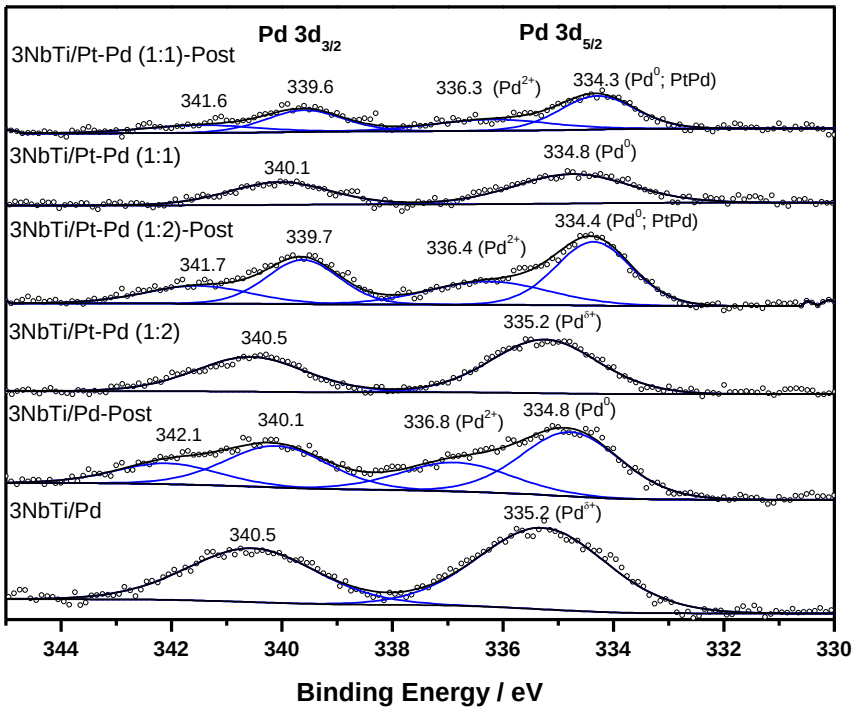

Figure 7. Pd *3d* XPS spectra for initial and post-reaction stages of selected samples. The assignment of the Pd $3d_{5/2}$ peaks is included in the figure.

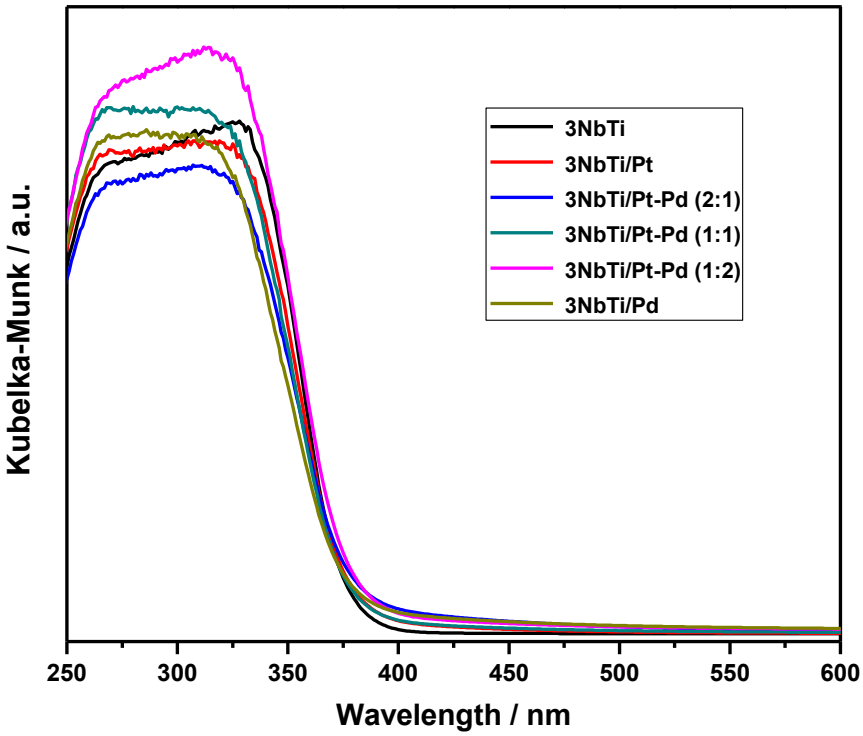

Figure 8. UV-visible spectra of the studied samples.

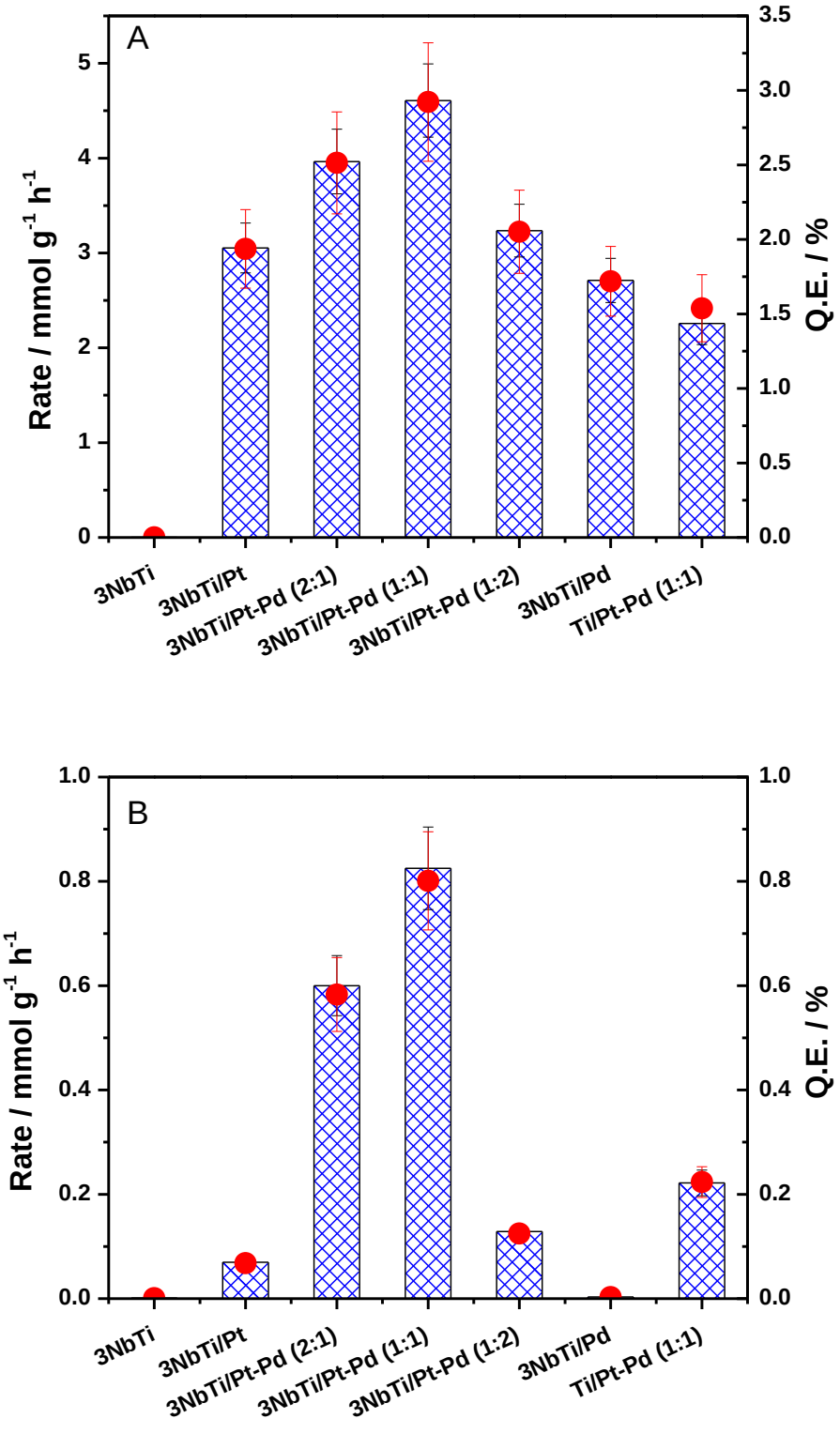

Figure 9. Reaction rates (bars) and quantum efficiency (circles) values obtained for the studied samples in the photo-production of hydrogen using a 3:7 CH_3OH:H_2O (v/v) ratio. (A) UV; (B) Visible illumination conditions.

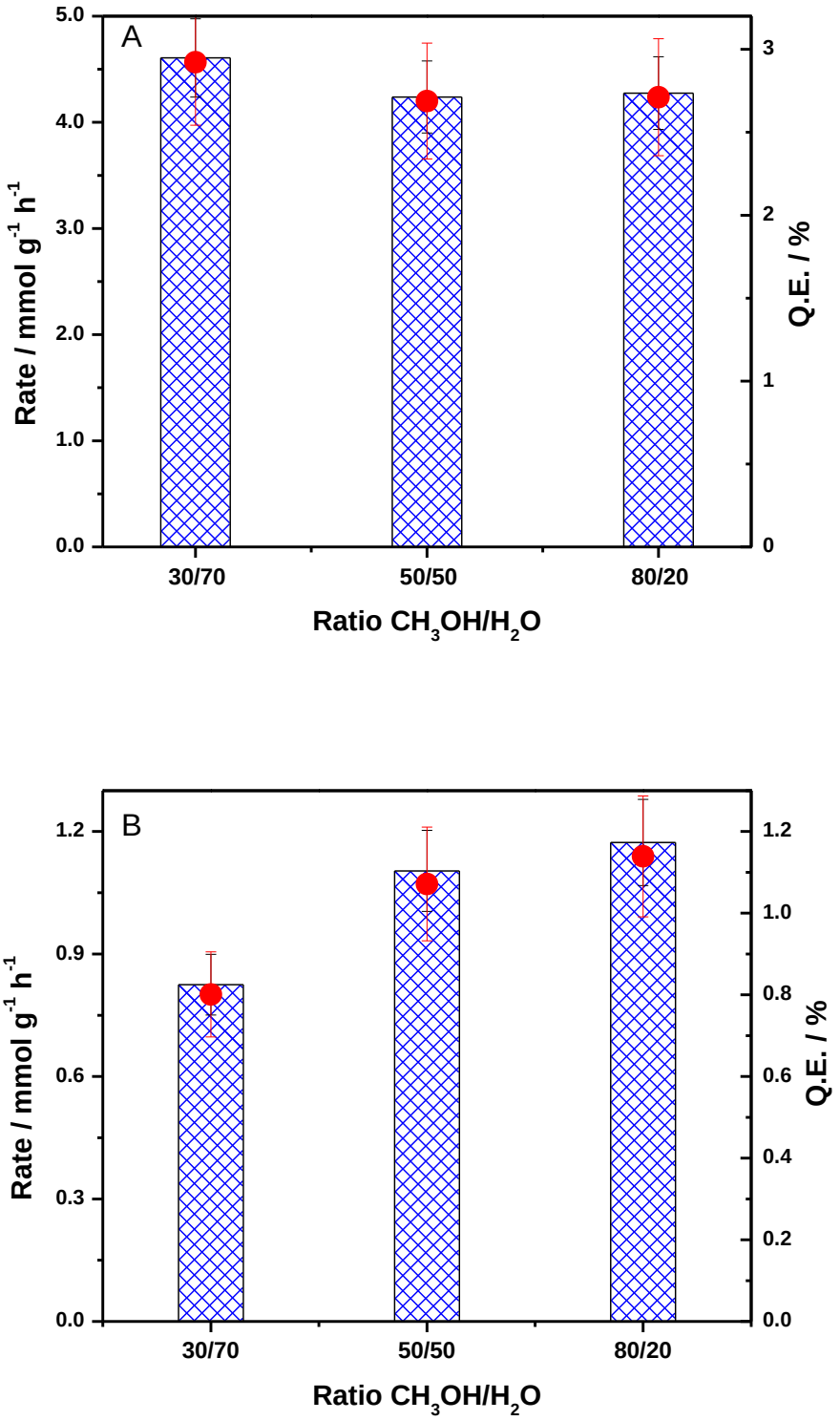

Figure 10. Reaction rates (bars) and quantum efficiency (circles) values obtained for the 3NbTi/Pt-Pd (1:1) sample in the photo-production of hydrogen using variable CH_3OH:H_2O (v/v) ratios. (A) UV; (B) Visible illumination conditions.

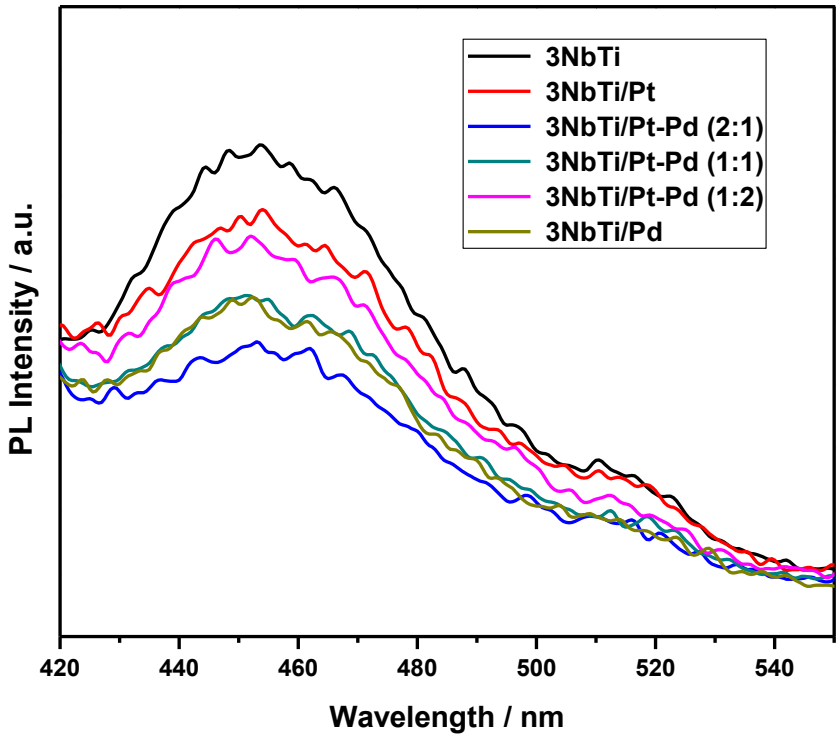

Figure 11. Photoluminescence spectra of the studied samples under 365 nm excitation.

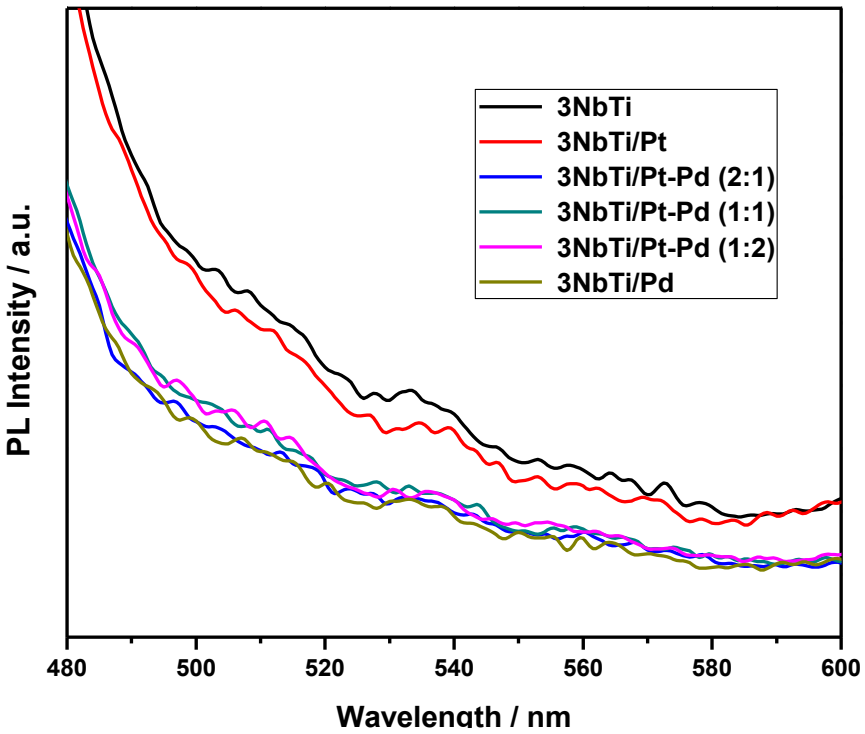

Figure 12. Photoluminescence spectra of the studied samples under 425 nm excitation.

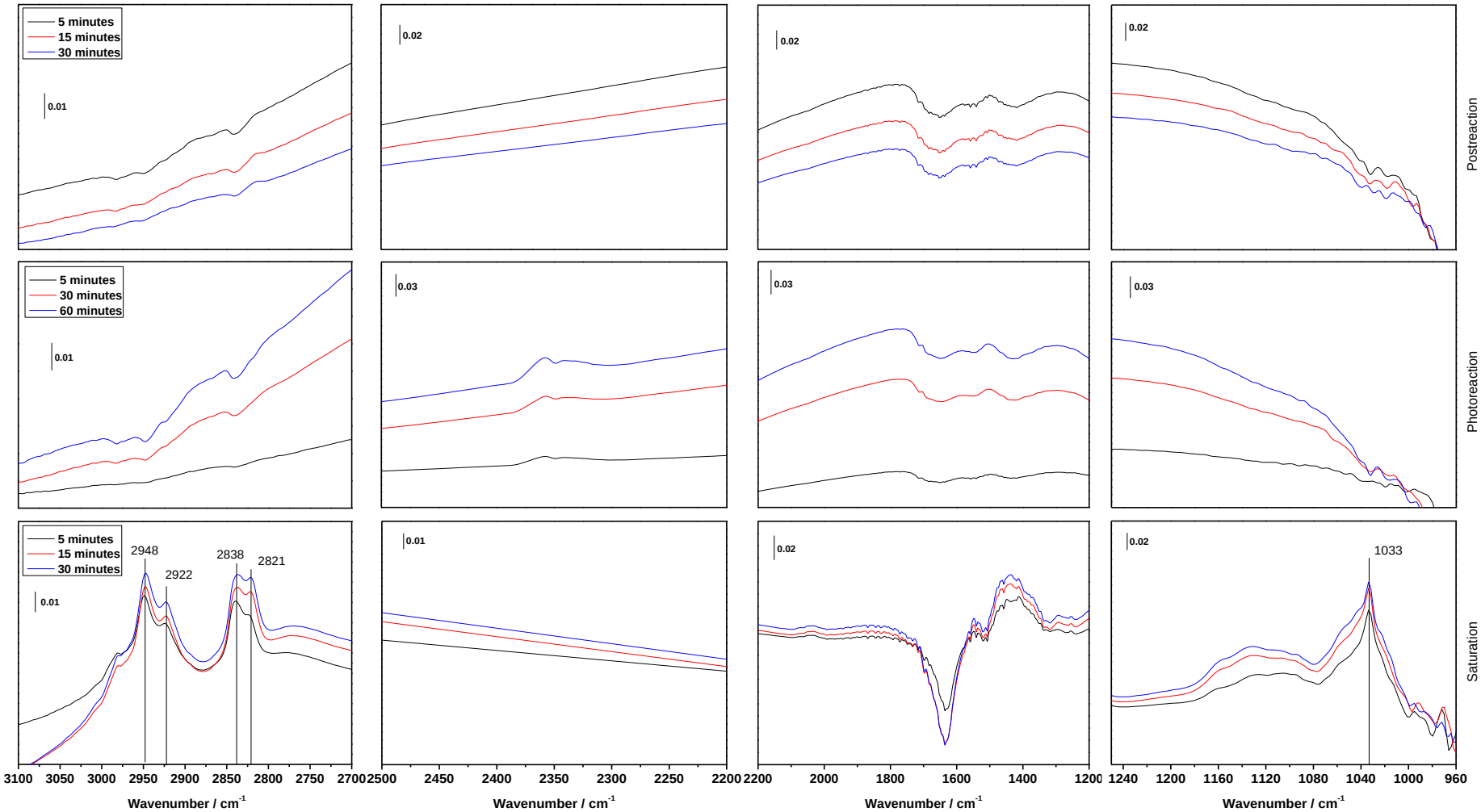

Figure 13. DRIFTS spectra of the methanol photo-transformation occurring under UV illumination for 3NbTi/Pt. Spectra obtained during saturation with the methanol:water (3:7 v/v) mixture, under reaction-illumination conditions and subsequently at dark conditions are presented.

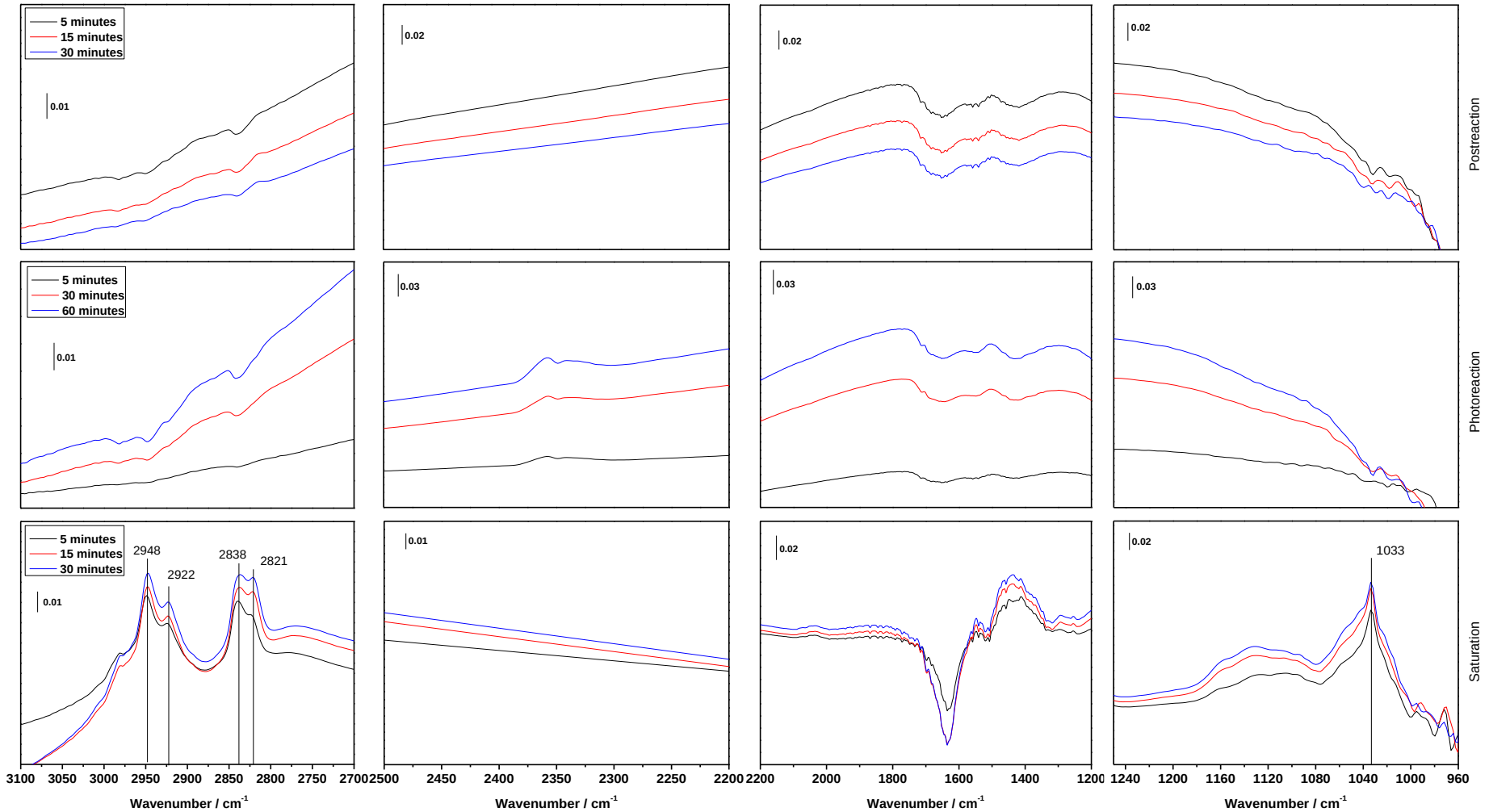

Figure 14. DRIFTS spectra of the methanol photo-transformation occurring under UV illumination for 3NbTi/Pd. Spectra obtained during saturation with the methanol:water (3:7 v/v) mixture, under reaction-illumination conditions and subsequently at dark conditions are presented.

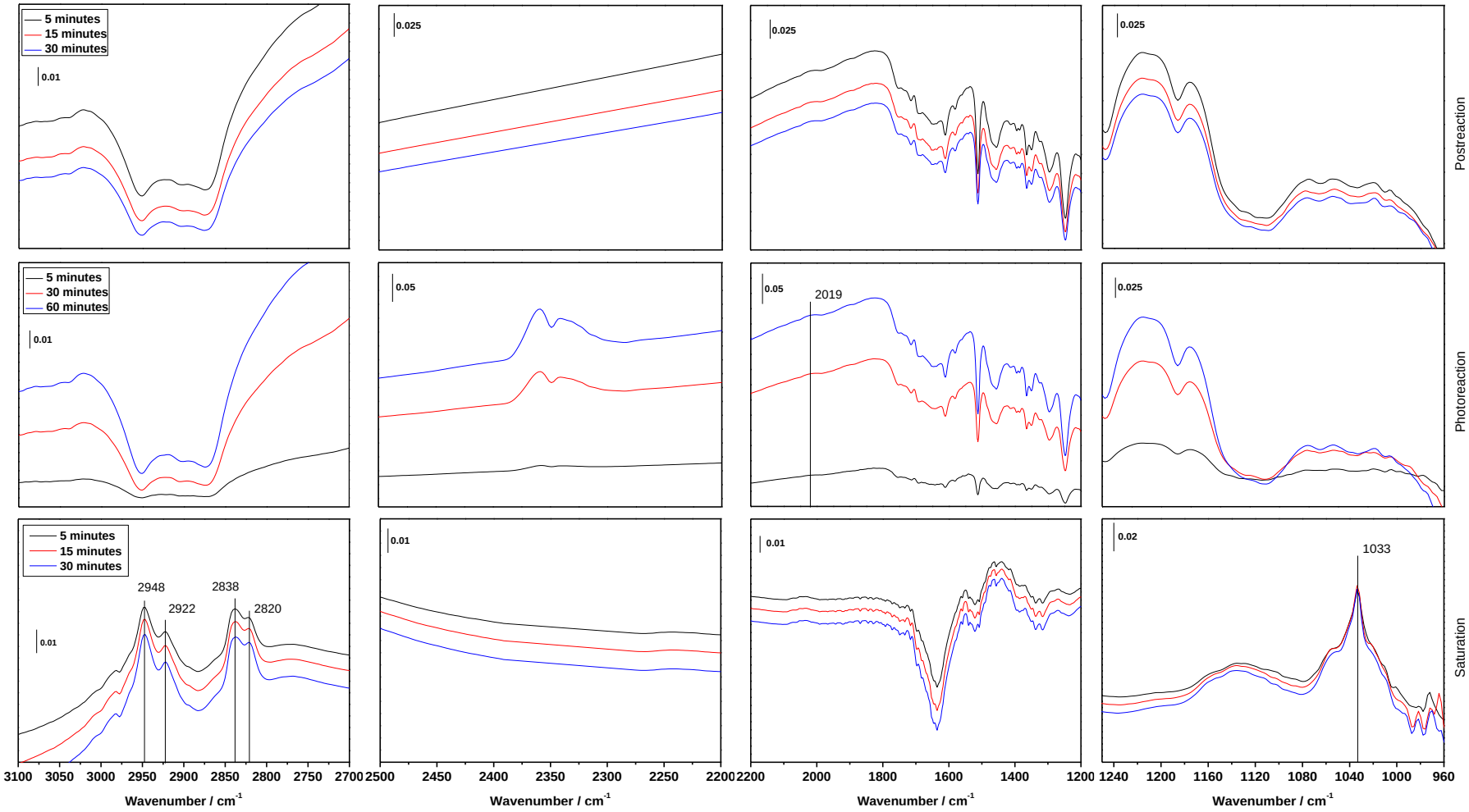

Figure 15. DRIFTS spectra of the methanol photo-transformation occurring under UV illumination for 3NbTi/Pt-Pd (1:1). Spectra obtained during saturation with the methanol:water (3:7 v/v) mixture, under reaction-illumination conditions and subsequently at dark conditions are presented.